ACS SENSORS

pubs.acs.org/acssensors Article

Smart Graphene Textiles for Biopotential Monitoring: Laser-Tailored Electrochemical Property Enhancement

Maxim Fatkullin, Vitaly Menzelintsev, Anna Lipovka, Elizaveta Dogadina, Evgenii Plotnikov, Konstantin Brazovskiy, Shuang Li, Lang Ma, Chong Cheng, Ekaterina Porokhova, Igor Khlusov, Li Qiu,* Raul D. Rodriguez,* and Evgeniya Sheremet

Cite This: *ACS Sens.* 2024, 9, 1809−1819 Read Online

ACCESS | Metrics & More | Article Recommendations | Supporting Information

ABSTRACT: While most of the research in graphene-based materials seeks high electroactive surface area and ion intercalation, here, we show an alternative electrochemical behavior that leverages graphene's potential in biosensing. We report a novel approach to fabricate graphene/polymer nanocomposites with near-record conductivity levels of 45 Ω sq^{-1} and enhanced biocompatibility. This is realized by laser processing of graphene oxide in a sandwich structure with a thin (100 μm) polyethylene terephthalate film on a textile substrate. Such hybrid materials exhibit high conductivity, low polarization, and stability. In addition, the nanocomposites are highly biocompatible, as evidenced by their low cytotoxicity and good skin adhesion. These results demonstrate the potential of graphene/polymer nanocomposites for smart clothing applications.

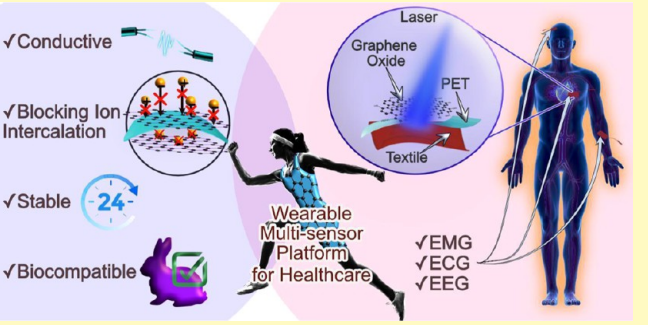

KEYWORDS: *reduced graphene oxide, electrochemistry, laser processing, skin biocompatibility, graphene/polymer composites, textile bioelectrodes, wearable healthcare devices, smart clothing, smart textiles*

Cutting-edge technologies in healthcare revolutionize patient monitoring and personalized health management.[1,2] The demand for real-time insights into a person's well-being fuels the development of sensors, enabling continuous, noninvasive monitoring of vital signs through biopotentials. While invaluable, traditional bioelectrodes and monitoring devices often fall short of delivering comprehensive and timely data, which are essential for informed medical decisions. Challenges include the intricacies of placing electrodes so that they do not lose contact with the skin and the cumbersome nature of the devices that can hinder patient compliance.

Addressing these challenges, our study introduces a novel approach to developing wearable bioelectrodes that are reliable and comfortable for continuous monitoring, which requires long-term stability under dynamic conditions. In this case, a primary concern is ensuring the safety of these electrodes during prolonged skin contact while simultaneously meeting clinical standards for signal quality and user comfort. Ideally, these monitoring devices should seamlessly integrate into daily life as accessories.

Many existing materials cause skin irritation, limiting their wearability for extended periods. Electrodes for biopotential registration must enable long-term use without the need for replacement or the introduction of conductive gels. Currently, the common standard for bioelectrodes is Ag/AgCl, which requires a gel to decrease contact resistance, limiting their use to 24 h.[13] Unfunctionalized metals cannot serve as an alternative as they are prone to electrical polarization, compromising the electrode performance for biopotential recording.

Laser-reduced graphene oxide (GO) has been recognized since 2009 as a powerful method for creating custom-shaped conductive patterns on different substrates.[5] The laser-induced rapid energy transduction triggers a swift temperature rise, material expansion, and release of CO_2, CO, and H_2O gases due to oxygen group removal. These quick transformations culminate in a highly porous reduced graphene oxide (rGO) surface with an increased interlayer spacing (3.49 vs 3.35 Å compared to graphene), thereby boosting the diffusion of ions into its structure.[3,6,7] These features result in the superior performance of laser-reduced GO compared to thermally reduced GO, particularly in supercapacitor applications.[4,6] Additionally, graphene-like materials have the potential to help

Received: November 6, 2023
Revised: February 28, 2024
Accepted: March 26, 2024
Published: April 8, 2024

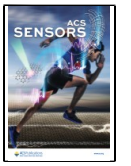

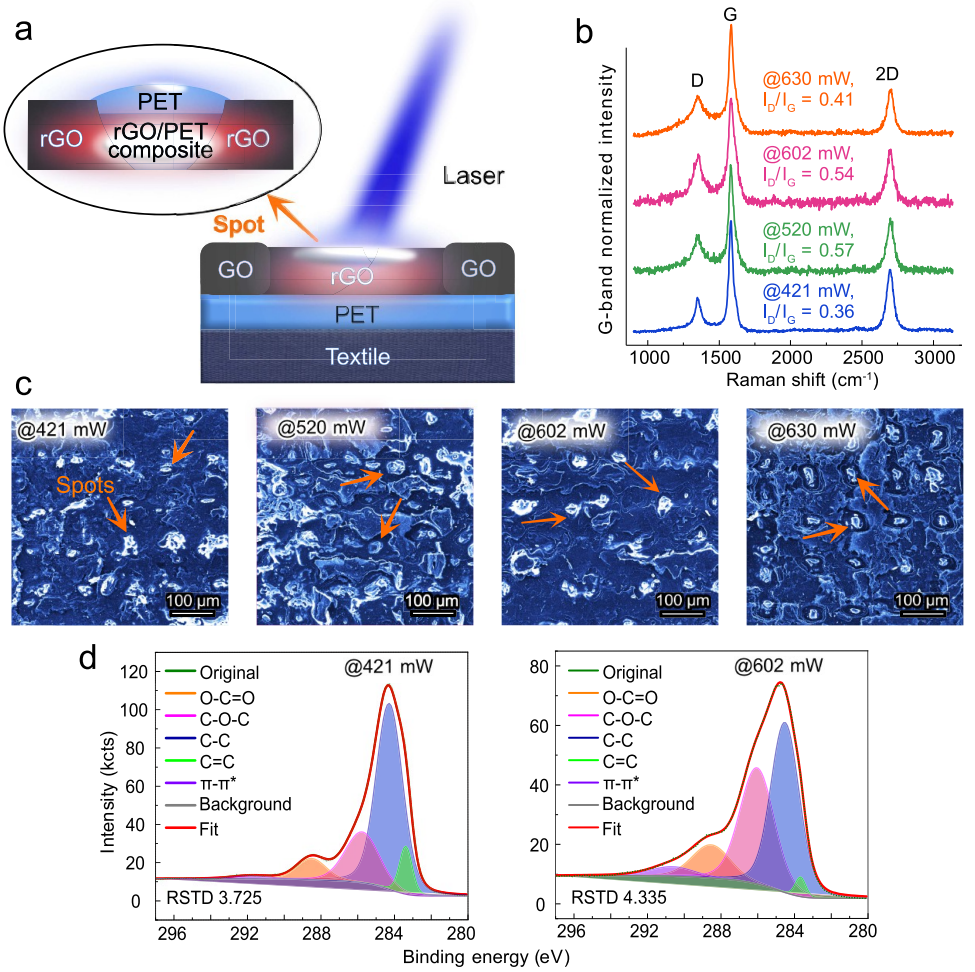

Figure 1. (a) Sketch of the sample structure and laser irradiation profile. (b) Raman spectra recorded from electrodes made with different laser irradiation conditions and the D/G Raman intensity ratios for each electrode. (c) SEM images from different electrodes. The arrows show regions (spots) with light contrast in the secondary electron imaging. (d) C 1s region XPS spectra for @421 and @602 mW electrodes.

avoid skin irritation and have already proved they could serve as dry bioelectrodes.[17]

The properties of rGO present exciting prospects in biomedicine and smart textiles.[8−11] Zhao et al. demonstrated a highly porous conductive rGO (90.6 ± 3.9 Ω sq^{-1}) transferred to PDMS, exhibiting an exceptionally large electroactive surface area ideal for the electrochemical detection of *Escherichia coli* with a limit of detection of 283 CFU/mL in artificial urine.[12] Beyond sensing, the next generation of electrodes for biopotential recording is critical for heart disease monitoring and athlete performance tracking.

In this study, we introduce laser processing to reduce GO on the surface of a polyethylene terephthalate (PET)/textile sandwich. This novel integration into textiles offers a versatile means to fix electrodes to the skin without adhesives. Building on our previous research,[14−16] we used laser processing to craft an rGO/PET/textile hybrid material, resulting in a robust, washable textile-based structure with significantly reduced electrode polarization, compared to the previous work.[17] This occurs thanks to blocking ion intercalation into the interlayer spacing of rGO with melted polymer, exposing only the topmost layers to the electrolyte. One of the most critical outcomes of this work is the exceptional biocompatibility of our material and its resilience against common daily wear factors.

This study brings new fundamental knowledge to the development of wearable bioelectronics and personalized healthcare and emphasizes real-world health applications of our bioelectrodes.

RESULTS AND DISCUSSION

Our approach to developing composite bioelectrodes is inspired by our previous findings[11,14,15] and involved three fabrication steps: first, a 100 μm thick PET sheet was thermally blended with a textile made of 90% polyester and 10% cotton; second, this sandwich was coated with a GO film. This nuanced change—the simultaneous use of textile and polymer—although simple, diverges from previous methods reported before. We found that this modification in electrode preparation maximizes electrical conductivity, durability, and biocompatibility while minimizing polarization effects. Third, laser processing was used to simultaneously reduce GO and embed it into the PET/textile matrix to create the final composite. During this process, GO served as both a graphene precursor and a photothermal transducer, where the high photon flux removed oxygen-containing groups. Simultaneously, the photothermal transduction in GO and rGO melted the PET substrate, allowing the intermixing of rGO flakes with the polymer matrix to occur in a liquid phase. This resulted in a robust conductive composite material seamlessly integrated

https://doi.org/10.1021/acssensors.3c02361
ACS Sens. 2024, 9, 1809−1819

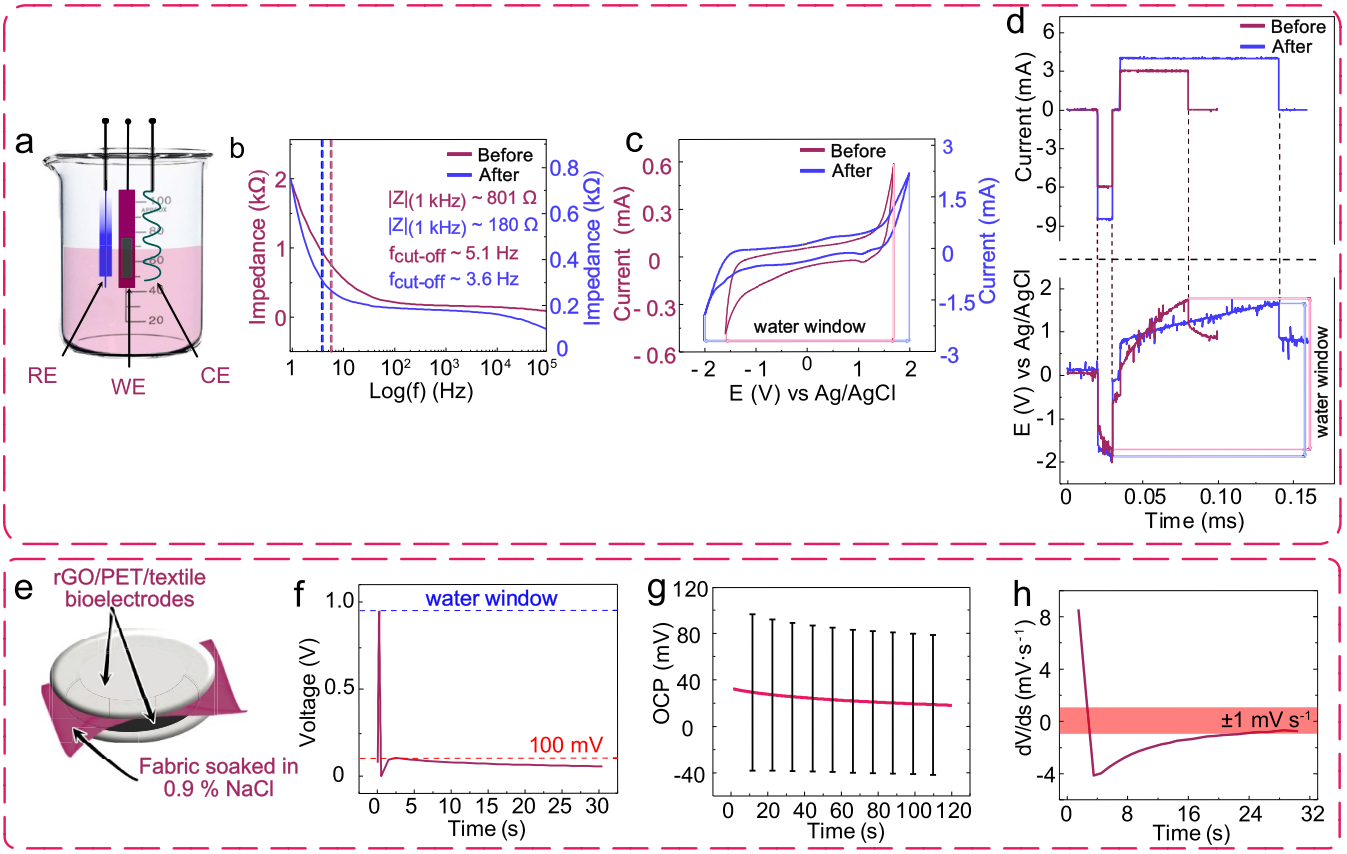

Figure 2. Electrochemical characterization of @602 mW bioelectrodes. (a) Sketch of the electrochemical cell. (b) Bode plots before (purple curve) and after (blue curve) 10 000 pulse load. (c) Cyclic voltammograms before (purple curve) and after (blue curve) 10 000 pulse load. (d) Charge-balanced stimulation before (purple curve) and after (blue curve) 10 000 pulse load. (e) Sketch for gel-to-gel electrode connection. (f) Defibrillation cycle and residual polarization after it. (g) Averaged from 12 pairs of electrodes residual polarization curve after AC stimulation. (h) Residual polarization change rate speed after defibrillation.

into textiles for wearable bioelectrode applications. The actual samples are shown in Figure S1.

Mechanism of Laser-Induced Composite Formation. In this work, GO reduction via laser processing was achieved through photothermal and, to a lesser extent, photochemical paths. The photothermal mechanism plays a key role in facilitating the composite formation between the rGO and the polymer substrate. During laser irradiation, GO absorbs light, which is then converted into heat, leading to the transformation of GO to rGO. As rGO darkens, it absorbs more light, increasing the photothermal transduction efficiency of the film.[18] This localized heating causes the PET substrate to melt, allowing the integration of rGO flakes into the molten PET matrix. After the laser is switched off, PET rapidly cools, resulting in solidification of the substrate with integrated graphene layers. Essentially, two simultaneous processes occur: the reduction of GO and the formation of the rGO/PET/textile composite (Figure 1a).

Laser power determines the extent of GO reduction and, consequently, the properties of the resulting rGO.[19] Here, we used four different integral laser powers (421, 520, 602, and 630 mW) to assess their effect on the properties of the rGO/PET/textile composite (data for these electrodes are summarized in Table S1). These power values were selected based on experimental optimization criteria that ensured the formation of mechanically stable and electrically conductive structures.

To investigate the properties of rGO, we used Raman spectroscopy, a powerful tool for analyzing carbon materials.[20] Raman spectra were collected from all of the electrodes produced with different integral laser powers (Figure 1b). All spectra displayed the typical bands of rGO: the defect-activated D band around 1350 cm^{-1}, the G band associated with sp^2 hybridized carbon around 1583 cm^{-1}, and the 2D band around 2700 cm^{-1}. The intensity ratio between D and G bands (I_D/I_G) reflects the level of graphene-like structure recovery (the lower the I_D/I_G, the less defective the rGO). Electrodes produced with an integral laser power of 421 mW had the lowest I_D/I_G of 0.36 ± 0.07. As the integral power increased, the I_D/I_G slightly increased to 0.57 ± 0.16, indicating the introduction of more structural defects. The same I_D/I_G of 0.54 ± 0.09 was observed for 602 mW. Surprisingly, a further increase in power to 630 mW decreased I_D/I_G to 0.41 ± 0.11. We explain these changes below.

The temperature achieved during laser processing of GO films depends on the applied laser power, with the values ranging from a few dozen to 2000 °C.[21,22] Along with GO reduction, the high temperature also causes changes in PET. At around 260 °C, PET starts to melt. As the temperature increases, the polymer viscosity decreases, leading to better intermixing with rGO, as observed in previous high-speed video studies of laser processing of functionalized graphene.[14] Additionally, higher temperatures lead to more intense polymer destruction and the release of hydrophilic byproducts on the surface.[14] When the temperature reaches the PET

https://doi.org/10.1021/acssensors.3c02361
ACS Sens. 2024, 9, 1809−1819

pyrolysis point (~500 °C), the topmost boundary of PET undergoes local carbonization, resulting in the formation of different carbon species, such as amorphous carbon and laser-induced graphene, within the rGO network. However, the molten PET must reach the lowest possible viscosity before this transformation begins.

Scanning electron microscopy (SEM, Figure 1c) revealed that the smoothest and most homogeneous electrode surface was achieved with a laser power of 602 mW. This observation suggests that this power level allows for the most effective integration of rGO into the PET matrix.

This conclusion is further confirmed by comparing the XPS C 1s regions from the electrodes produced under 421 and 602 mW laser powers (Figure 1d). The intensity ratios between the peaks assigned to C−O−C (~286 eV) and C−C (~284.5 eV) bonds[23] significantly differ, with a higher ratio for 602 mW. This is clear evidence that there is more polymer on the surface of the 602 mW electrode but with a higher degree of GO reduction, as indicated by the higher $\pi-\pi$ satellite. This XPS peak and the lowest sheet resistance (45 Ω sq^{-1} for 602 mW vs 70 Ω sq^{-1} for 421 mW) both originate from delocalized electrons. This indicates that the 602 mW laser power is close to the temperature required to reach the lowest viscosity for liquefied PET. Across all electrode surfaces, we observed laser patterns characterized by a PET-rich region at the center of the laser spot, surrounded by rGO, as schematically depicted in Figure 1a. This PET spot forms due to the laser-induced melting of the polymer and its subsequent resolidification.

Based on our observations from XPS and SEM, we conclude that the unexpected changes in the I_D/I_G ratios can be attributed to the integration of high-quality graphene into PET. Only the poorly reduced parts at the periphery of the laser spot are present on the surface and left exposed to the Raman laser.

Electrochemical Characterization. To translate into actual applications, the bioelectrodes must meet the requirements for biomedical devices. That is why we further focused on elucidating and understanding their electrochemical properties, following the guidelines outlined in Nature Protocols by Boehler et al.,[24] using a three-electrode cell, as sketched in Figure 2a.

Impedance Aanalysis. First, we conducted impedance measurements using rGO/PET/textile bioelectrodes created with different integral laser powers (Figures 2b and S2). The parameters extracted from the Bode plot were evaluated, including the impedance value at 1 kHz frequency and the cutoff frequency (f_{cutoff}). All electrodes met the requirement of having an f_{cutoff} below 1 kHz. Our results show that increasing the integral laser power affects the cutoff frequency and decreases the impedance value at 1 kHz $|Z|_{1\ kHz}$ because of the higher temperature under laser irradiation and the degree of rGO reduction.

Cyclic Voltammetry (CV). We obtained CV curves from each electrode in Dulbecco's phosphate buffered saline (DPBS), a commonly used electrolyte that simulates human body fluids. Figures 2c and S3 show that the reduction peak was observed at around −0.6 V for all laser powers, indicating that GO was not fully reduced during laser processing. This peak was attributed to the removal of oxygen-containing residues from laser-reduced GO.[25] A small oxidation peak was visible for all electrodes except for @602 mW, suggesting that mass transfer limitations prevented the oxidation process. We calculated the maximum charge storage capacity (CSC_{max}) and areal capacitance (C_{areal}) for different electrodes. The results showed that the 602 mW rGO/PET/textile bioelectrodes behave differently from the rest. Increasing the laser power from 421 to 520 mW increased capacitance from 0.6 to 2.2 mF cm^{-2} due to a higher reduction. However, for 602 mW electrodes, the areal capacitance dropped to 1.9 mF cm^{-2} and then rose again to 2.9 mF cm^{-2} when the power increased to 630 mW. All values for areal capacitance are comparable to the state-of-the-art for laser-reduced GO.[26,27]

Correlation with Surface Structure. SEM results in Figure 1c suggest that changes in areal capacitance are linked to the surface structure. Therefore, we attribute the capacitance drop for 602 mW electrodes to the most effective integration of rGO into PET. This enhanced surface intermixing likely blocks mass transfer to the active sites.

Water Window Potential. The value of the water window potential is an essential parameter for bioelectrodes as it defines the safe operational potential range to avoid irreversible changes in the surrounding environment. Our observations of the water window showed a similar trend as the areal capacitance: the 602 mW electrodes deviated from others, shifting the electrolysis potential toward zero with increasing laser power. We attribute this result to the higher degree of reduction, which leads to a higher electroactive surface area. The changes in the water window for 520 mW electrodes were as expected, but for 602 mW, the water window widened, which was attributed to the same processes affecting the areal capacitance. There was a downshift in the water window at 630 mW (Figures 2c and S3).

Charge-Balance Stimulation (CBS). To mimic the pulsed nature of biosignals, we conducted CBS tests, assessing the maximum charge injection capacities (CIC_{max}) for both cathodic and anodic phases and ensuring that voltage did not exceed the water window potential. CBS for all electrodes was performed with leading cathodic and compensational anodic current-controlled pulses (Figures 2d and S4). The results showed that the CIC_{max} for the leading pulse increased with increasing power until 602 mW (60.7 μC for the cathodic phase and 135.8 μC for the anodic phase) but slightly dropped for the 630 mW electrode. It is likely that the 630 mW electrode did not have a different behavior but the 602 mW required more charge injection to reach the water window. Additionally, the CBS tests showed that even though 602 mW electrodes had the highest CIC_{max} for the cathodic phase, they also had the lowest CIC_{max} for the anodic (compensatory) pulse. These observations support the conclusion that mass transport is blocked by the intermixing of graphene with the polymer matrix and the unique behavior of the 602 mW electrode compared to others.

Real-Life Performance. We tested our bioelectrodes, simulating realistic conditions during a continuous pulse load test and setting the same parameters as for the CBS test. After 10 000 pulse load cycles, CV analysis revealed an oxidation peak for the 602 mW electrode (Figure 2c) and increased overall current values for all electrodes. This indicates that rGO was further electrochemically reduced beyond the state achieved through laser reduction (Figure S5), as confirmed by the XPS analysis. After the pulse load, the 602 mW electrode shows a decreased intensity ratio between the C−O−C and C−C peaks (Figure S6). This electrochemical reduction of rGO caused a reversible redox reaction at the electrode surface. The oxidation peak suggests that oxygen species can reach the active sites on the electrode surface and form bonds, leading to the cyclic oxygen functionalization of rGO during EC

https://doi.org/10.1021/acssensors.3c02361
ACS Sens. 2024, 9, 1809−1819

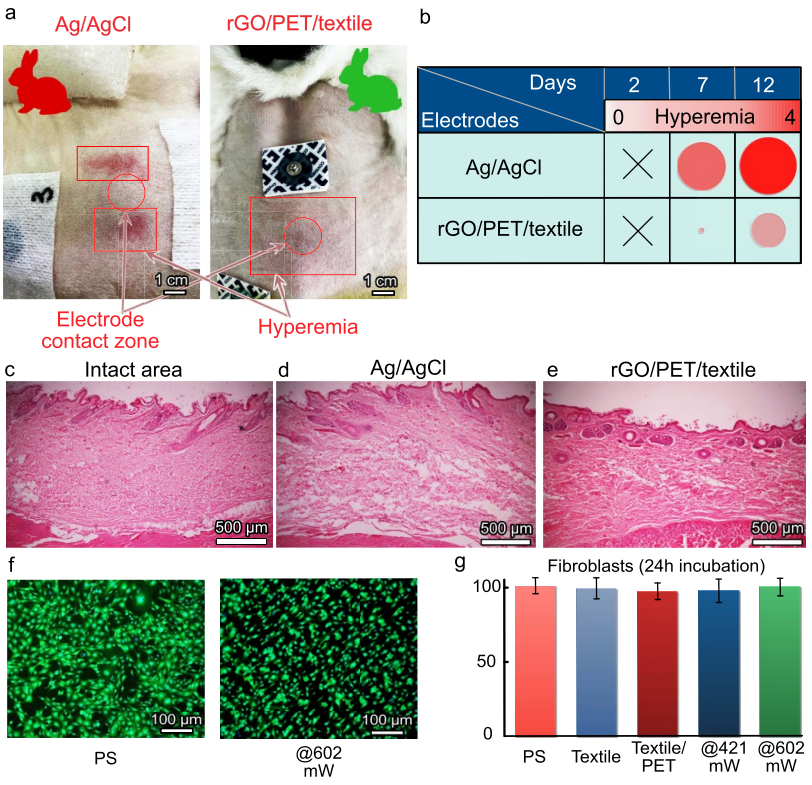

Figure 3. Biocompatibility study results. (a) Pictures of rabbit's skin under the commercial Ag/AgCl electrode and @602 mW rGO/PET/textile bioelectrode. (b) Averaged semiquantitative visual (macroscopic) analysis of rabbit's skin after 2, 7, and 12 days of contact for Ag/AgCl electrodes and @602 mW rGO/PET/textile bioelectrodes. The circle size represents the relative hyperemia surface, and the color-coded scale represents hyperemia intensity. (c–e) Microscopic images of skin cut from the intact area, the area under the Ag/AgCl electrode, and under the rGO/PET/textile bioelectrode, respectively. (f) Fibroblast cell proliferation fluorescence microscopy images for cultures on a standard polystyrene Petri dish and on the @602 mW rGO/PET/textile bioelectrode. (g) Cell viability comparison.

sweeping.[28] The improvement in the capacitance of all electrodes was likely caused by the electrochemical reduction of rGO and an increase in surface roughness, resulting in lower impedance values at low frequencies, where capacitance is the dominant factor. It is important to clarify that the electrochemical modifications observed in rGO/PET/textile electrodes do not impact their performance in the intended applications. This is due to the significantly lower biopotential signal amplitudes compared with those used in stimulation. This observation is not only relevant for the current application but also opens avenues for further research into the electrochemical behavior of rGO/PET/textile composites.

Postload Testing. After repeating the CBS test following 10 000 pulse loads (Figure S7), we observed the same changes as in the CV results. The CIC_{max} values increased for both phases across all electrodes, especially for the compensational pulses, with the smallest changes observed for the 602 mW electrodes (Figure 2d). This trend confirms the unique behavior of 602 mW electrodes with the highest CIC_{max} for the leading pulse and the lowest for the compensational pulse.

Gel-to-Gel Bioelectrode Assessment. To ensure the efficacy of bioelectrodes when in direct contact with the skin, we evaluated their performance and stability using a gel-to-gel connection, following the American standard for ECG electrodes.[29] Gel-to-gel connection is a widely used electrode–skin contact model to directly indicate electrode performance, omitting personal factors. Since our electrodes do not require gel, the skin–electrode contact was simulated by a fabric soaked in saline (Figure 2e).

Performance criteria:

(1) Open-circuit potential (OCP): The American standard for ECG electrodes mandates that the OCP between two gel-connected electrodes should not exceed 100 mV for 30 s after alternating current (AC) stimulation. Our tests in 12 electrode pairs, fabricated using different laser powers, revealed that only the 602 mW electrodes passed this requirement. All of the others exceeded the 100 mV limit (Figures 2f and S8a).

(2) OCP postdefibrillation pulse: The OCP should not exceed 100 mV for 60 s after a defibrillation pulse (charge–discharge cycle). The 602 mW electrodes showed the lowest residual polarization below 100 mV, while the other electrodes had much higher values (Figures 2g and S8b). By surpassing the value of 100 mV, we conclude that our electrodes could not be used either for defibrillation or real-time ECG monitoring during defibrillation.

(3) OCP rate of change postdefibrillation: The rate at which OCP changes during 60 s after defibrillation must not exceed ± 1 mV s^{-1}. Unfortunately, none of our electrodes met this criterion (Figures 2h and S8c), supporting the conclusion that the electrodes cannot be used for defibrillation purposes.

(4) Impedance at 10 Hz: The impedance value at 10 Hz should not exceed 3 kΩ. All electrodes fabricated in this work successfully met this criterion, indicating that all of them have appropriate electrode/skin impedance (see Table S1). We performed a comparative test with Ag/

https://doi.org/10.1021/acssensors.3c02361
ACS Sens. 2024, 9, 1809–1819

AgCl electrodes. The measured impedance at 10 Hz had a value of 84.1 ± 9.5 Ω, being notably lower than that observed for rGO/PET/textile bioelectrodes. Despite this substantial difference, this does not anyhow limit the targeted application performance of our electrodes in ECG.

It is essential to note that the impedance measurements for Ag/AgCl electrodes were conducted in accordance with their typical usage, which means incorporating conductive gel to reduce interfacial impedance. At the same time, our electrodes were tested without the use of gel.

Insights from Electrochemical Analysis. The electrochemical tests revealed that electrodes produced with a laser power of 602 mW exhibited different behaviors compared to other electrodes produced with different laser powers. The 602 mW electrodes consistently showed a low polarizability across all tests. We attribute this to the higher laser power causing more extensive polymer melting, leading to greater penetration of rGO flakes into the polymer matrix. Meanwhile, laser powers higher than 602 mW are sufficient to induce PET pyrolysis,[15] creating laser-induced graphene with a more conductive carbon network and higher surface roughness—factors that increase polarizability, an undesirable characteristic for bioelectrodes. Conversely, high temperatures, but still below the pyrolysis threshold, can lead to partial polymer destruction and removal of the topmost conductive rGO layers due to laser ablation. This scenario results in an electrode surface covered mainly by PET and its decomposition products, which interrupts ion intercalation, a primary mechanism of charge storage in graphene,[30,31] which explains the low polarizability observed in the 602 mW electrodes.

Advancing Smart Clothing: Biocompatibility Tests. The biocompatibility of our 602 mW bioelectrodes was evaluated with animal tests. We placed three rGO/PET/textile electrodes on rabbit skin and compared them with three hypoallergenic Ag/AgCl electrodes over a 14-day period. Ag/AgCl electrodes remain a golden standard and represent the only commercially available solution up to now. While the hypoallergenic electrodes were replaced daily according to the manufacturer's recommendations, our rGO electrodes remained in place throughout the whole period, with only the adhesive patches being changed daily. Notably, the skin under the commercial electrodes exhibited signs of irritation, particularly at the electrode/patch interface, which worsened over time (Figure 3a). This irritation is likely due to the glue in the commercial electrodes, which can cause friction with the hard Ag/AgCl electrode material, exacerbated by the rabbit's movements.

Conversely, our electrodes showed no skin inflammation or damage. However, some poorly integrated rGO flakes detached from the electrodes on the second day, leaving a temporary gray stain on the skin. This suggests the need to optimize the composite formation to prevent flake transfer, possibly by washing the electrodes instead of only rinsing them before use. Slight signs of skin irritation were observed around the target electrodes, likely caused by adhesive patches (Figure 3a).

Semiquantitative Skin Reaction Analysis. We performed a semiquantitative examination of the skin reaction around each electrode, as presented in Figure 3b and Table S2. We graded the degree of hyperemia on a scale from 0 (no reaction) to 4 (severe reaction), as represented by the circle area in Figure 3b. Statistical analysis according to the Mann−Whitney test confirmed the lighter external injury of the skin by rGO/PET/textile electrodes (@602 mW; Table S2).

Histological Skin Analysis. Histological examination of the skin revealed that while intact skin showed no damage (Figure 3c), the Ag/AgCl electrodes caused noticeable harm. The skin damage included loosening of the dermis and destruction of collagen fibers as well as a decrease in the number of hair follicles in the reticular layer of the dermis (Figure 3d). In contrast, microscopic observation (Figure 3e) of the dermis in contact with rGO/PET/textile bioelectrodes showed no graphene infiltration and less severe fibrous component damage than Ag/AgCl according to semiquantitative estimation (see Table S3).

Leukocyte Infiltration. We observed some degree of leukocyte infiltration in all of the skin samples. However, only individual leukocytes and small clusters were found in intact areas of the skin. The infiltrate's cellular component was mainly mononuclear leukocytes (monocytes and lymphocytes); neutrophils and eosinophils were also present in small quantities (Figure S9a). In the rabbit skin dermis under Ag/AgCl electrodes, we observed large foci of leukocyte infiltration, mainly consisting of segmented (possibly stab) neutrophils and mononuclear macrophages (Figure S9b). Semiquantitative analysis showed a 2-fold increase in leukocyte infiltration compared with intact skin (median 2 points versus 1 point in intact skin, Pu = 0.001). In turn, an intermediate level of leukocyte infiltration was observed between Ag/AgCl and intact zones (Figure S9c), with the infiltrate mainly composed of macrophages and eosinophils. The composition of the leukocytes indicates that the rGO/PET/textile bioelectrodes caused only mild irritation. Conversely, Ag/AgCl electrodes appear to induce marked, nonspecific inflammation across the layers of skin in contact with them.

Impression Smear Microscopy. Microscopic examination of impression smears taken from intact skin showed no signs of inflammation (Figure S9d). Skin areas under Ag/AgCl electrodes showed large sheets of exfoliated stratum corneum (Figure S9e) and numerous nucleated epithelial cells from the deeper layers of the epidermis (Figure S9f). Ag/AgCl also resulted in a large number of leukocytes, mainly polymorphonuclear neutrophils and mononuclear cells, such as macrophages and lymphocytes (Figure S9g), indicating acute injury and inflammation of the skin. In contrast, skin under rGO/PET/textile electrodes showed no signs of epidermal trauma or leukocyte infiltration after 14 days of application, with only single horny scales present (Figure S9h).

Conclusion: Superior Biocompatibility of rGO/PET/Textile Electrodes. Skin rabbit analysis revealed that our bioelectrodes have far fewer unwanted side effects than commercially available Ag/AgCl electrodes, even though the latter were replaced daily. This suggests that our electrodes are suitable for long-term ECG monitoring and can be safely used without replacement for up to 6 days. However, extending the 6 day period does not cause any significant skin damage.

Graphene and its derivatives can cause cell membrane damage due to its sharp edges or oxidative stress.[32,33] However, the biocompatibility of graphene composites is higher than that of other forms of graphene[34] and can be expected even higher for composite structures, where graphene cannot freely infiltrate the cells.[34] We conducted cell proliferation tests comparing the cytotoxicity of rGO/PET/textile bioelectrodes, textile alone, and PET/textile (without

https://doi.org/10.1021/acssensors.3c02361
ACS Sens. 2024, 9, 1809−1819

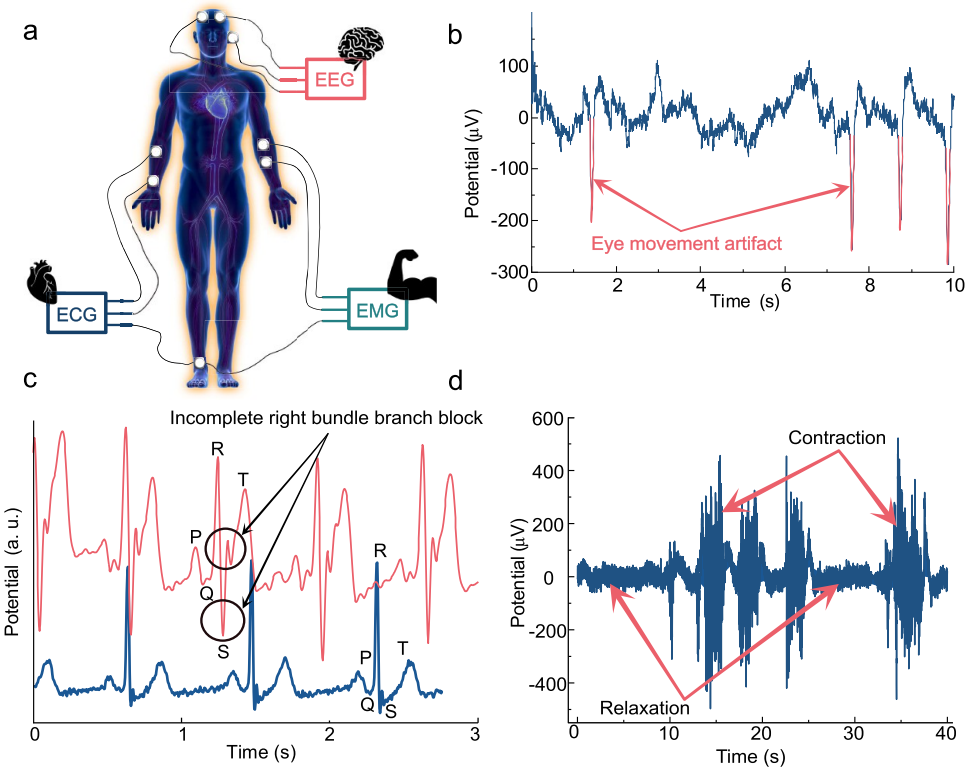

Figure 4. Tests for smart cloth application. (a) Sketch of the EEG, EMG, and ECG measurements. (b) EEG signal with opened eyes. (c) ECG recorded using @602 mW rGO/PET/textile bioelectrode: normal ECG (blue line) and ECG with incomplete right bundle branch block (red line). (d) EMG recorded using @602 mW rGO/PET/textile bioelectrodes.

GO or rGO) against standard polystyrene (PS) Petri dishes used for cell culture experiments. After 24 h of cell culture, we observed cell growth in all samples and the cytotoxicity test revealed no significant differences (p-value<0.05) in cell viability in all groups vs control (Figures 3f,g and S10). Cell viability was within 96−99% of the control group (according to the MTT test protocol). This suggests that no toxic components were released and no significant cell oxidative stress damage occurred, verifying the excellent biocompatibility of all samples. The difference in cell growth density on the surface is attributed to the distinct sample morphology; the textile structure without coating did not allow cells to grow evenly to form a layer, significantly reducing the density per unit surface area compared to the control (standard culture plate).

Chemical and Mechanical Stability. To ensure the practical application of our bioelectrodes in smart clothing, we conducted tests to simulate real-life conditions, focusing on their interactions with sweat, washing processes, and mechanical bending.

Sweat Resistance. We first investigated the electrodes' resistance to sweat by immersing them in artificial sweat. The sheet resistance was measured before and after sweat exposure to evaluate their stability. All electrodes demonstrated excellent stability, with insignificant changes in sheet resistance values after soaking in acidic artificial sweat (Figure S11a). Notably, the sheet resistance for most electrodes, except for at 421 mW, actually decreased. This suggests that the sweat immersion helped remove loosely bound flakes and PET decomposition products from the electrode surface.

Washing Durability. Next, we tested the electrodes' stability to withstand washing in an alkaline soap solution, a crucial factor for smart clothing applications. As shown in Figure S11b, the sheet resistance of 421, 520, and 630 mW electrodes initially decreased after the first wash but increased after the second. This change indicates the removal of residues and PET decomposition byproducts from the surface in the first wash but partial oxidation/removal of rGO during the second wash (Figure S11b). In contrast, 602 mW electrodes showed a consistent drop in sheet resistance after the first wash and then stabilized. This behavior indicates that the PET surface coverage effectively shielded rGO from the harsh chemical environment and mechanical detachment. Surface changes for 602 mW electrodes caused by washing were further investigated by SEM (Figures S12a and S11b) and EDX (Figure S13), revealing the presence of spherical nanoparticles from the soap and an increased chlorine content, indicating some residual substances.

Bending Stability. Finally, we evaluated the electrodes' stability through a bending test, simulating the wearer's motion. The electrodes maintained stable resistance values even after 1000 bending cycles with only a 5% variation between bent and unbent states (Figure S11c). This small resistance change is crucial as it minimizes motion artifacts caused by deformation, thereby enhancing the feasibility of integrating these sensor electrodes into smart clothing.

Conclusion: Robustness for Smart Clothing Integration. The implemented tests collectively demonstrate that our bioelectrodes possess the chemical and mechanical robustness required for their integration into smart clothing. They exhibit remarkable stability against sweat, retain functional integrity through washing cycles, and withstand physical bending, making them promising candidates for long-term, real-world applications in wearables.

https://doi.org/10.1021/acssensors.3c02361
ACS Sens. 2024, 9, 1809−1819

Application as an Electrode for Biopotential Readout. Our bioelectrodes have been successfully applied to capture various electrophysiological parameters. We conducted experiments to record a volunteer's electromyogram (EMG), electrocardiogram (ECG), and electroencephalogram (EEG), demonstrating the electrode's versatility (Figure 4a).

EEG recording: for EEG, we focused on the Fp1 and Fp2 sites (Figure 4b). The recordings showed a clear β rhythm, confirming the electrode's efficacy in biopotential recording. EEG spectra measured with rGO/PET/textile bioelectrodes were compared with those from Ag/AgCl electrodes via frequency domain analysis. The electrodes were found to be almost identical, and the difference between them does not exceed 0.15 μV^2 Hz^{-1} (Figure S14). *ECG recording*: we also recorded an ECG (Figure S15) using our rGO/PET/textile and commercial Ag/AgCl electrodes. Commercial Ag/AgCl electrode patches were selected as control electrodes since they are the standard for ECG recording in clinical settings as well as in research.[35−37] The particular Ag/AgCl electrodes used in this work are certified medical devices in accordance with Regulation (EU) 2017/745 (MDR). The comparison revealed consistent PQRST complexes and R−R intervals in both cases with no isoline drift. This indicates that our electrodes provide high-quality recordings comparable to those obtained with their commercial counterparts. *Detecting cardiac pathologies*: further, we tested the bioelectrodes' ability to detect cardiac abnormalities. ECGs were recorded from two volunteers: one diagnosed with an incomplete blockade of the right branch of the Hiss bundle and one without any known pathology (Figure 4c). The ECG from the volunteer with the pathology displayed distinct features, such as a notched S-wave, a merged ST-segment and T-wave, and a wider QRS complex (0.14 vs 0.12 s). These characteristics are indicative of the specific cardiac pathology, demonstrating our electrode's capability to detect such nonobvious changes. This is particularly critical for athletes, where early detection of cardiac issues is crucial. *EMG recording for muscle activity*: additionally, we recorded EMG by attaching rGO/PET/textile electrodes to the flexor carpi radialis muscle area. The resulting EMG graph in Figure 4d showed clear peaks corresponding to the muscle's tension and relaxation, effectively indicating the muscle's activity during hand movements.

Advantages over Other Wearable Electrodes. Our rGO/textile/PET electrodes exhibit several distinct characteristics when compared to other wearable electrodes for biopotential recording. Notably, the absence of gel ensures consistent electrical contact over time, as there is no risk of the gel drying out. This lack of gel may also contribute to reduced skin irritation. These electrodes are designed for prolonged use, and their performance metrics, as shown in Table S4, are competitive. The ability for prolonged use was confirmed by recording ECG using the electrodes before and after aging in PBS for 13 days at 37 °C (Figure S16). We did not observe any severe degradation in signal quality; however, the signal-to-noise ratio dropped by ∼7%, which is an acceptable deviation for such devices. Furthermore, our production method is both cost-effective and environmentally friendly, emphasizing the sustainable nature of our approach.

In addition, our wearable textile bioelectrodes are well-suited for a range of biopotential monitoring applications, including high-quality EEG, ECG, and EMG recordings. Their capability to detect specific cardiac conditions and muscle activities makes them invaluable in both clinical and athletic environments. The compatibility of these electrodes with smart clothing also highlights their potential for extended, non-invasive health monitoring.

CONCLUSIONS AND FUTURE OUTLOOK

Our research is centered on developing and investigating graphene−polymer composite bioelectrodes fabricated via laser processing on textile substrates, revealing their remarkable performance and stability for biosensing applications. We found that even slight variations in laser power significantly impacted the integration, primarily through photothermal polymer melting and graphene oxide reduction.

In contrast to previous work, we show the crucial role of incorporating an insulating polymer to mitigate polarization effects. The successful intermixing of reduced graphene oxide and polyethylene terephthalate effectively limits ion intercalation. This blocking mechanism was crucial in preserving the material's integrity and performance. Thus, the choice of optimal laser power not only results in stable electrode fabrication but also helps avoiding polarizability and deviation of electrical properties from electrode to electrode.

Our bioelectrodes exhibited exceptional mechanical, chemical, and electrical robustness, enabling their application in electrocardiography (ECG), electromyography (EMG), and electroencephalography (EEG). Notably, they surpassed the performance benchmarks set by the conventional electrodes. In vivo investigations further demonstrated the superior skin biocompatibility of our graphene-based electrodes, which inflicted minimal skin damage during prolonged use, in stark contrast to commercial hypoallergenic electrodes.

While our devices met nearly all of the criteria set by the American standards for bioelectrodes, they slightly missed the mark on the open-circuit potential changing rate, exceeding the ± 1 mV s^{-1} threshold. Nevertheless, leveraging on these new insights and concepts, we are now actively working toward translating our research into wearable devices, envisioning transformative advancements in bioelectronics.

Rigorous testing, including 1000 bending cycles, washing, and soaking in artificial sweat, revealed that our bioelectrodes retained their initial properties, demonstrating their potential for long-term use in smart clothing applications.

However, despite the evident advantages of our rGO/PET/textile bioelectrodes over commercial counterparts, potential movement artifacts could pose challenges in real-world applications. Currently, our technology seems particularly beneficial for athletes, who usually wear form-fitting attire, ensuring consistent skin contact without the need for adhesive patches. For the average user, even if an adhesive patch is needed, our electrodes have proven to be gentle to the skin, causing minimal irritation. In conclusion, our research has paved the way for innovative advancements in wearable bioelectronics, offering a promising alternative to traditional electrodes.

METHODS

This section briefly discusses the crucial methods and materials used, while more complete information can be found in Note S1 in the Supporting Information.

Bioelectrode Fabrication. First, the PET lamination film was attached to the textile by heating it to 100 °C, so the polymeric glue started to melt and merge PET and textile. The aqueous dispersion of GO (Graphene Inc., Spain) at 4 mg/mL was drop-casted on the hybrid PET/textile and dried at 50 °C. Further, the GO film was

https://doi.org/10.1021/acssensors.3c02361
ACS Sens. 2024, 9, 1809−1819

processed by using a computer-controlled pulsed diode laser with a 436 nm wavelength operating at 1.6 kHz frequency. The spot size was 350 × 150 μm^2. In this work, we used four integral powers for laser processing: 421, 520, 602, and 630 mW.

Characterization was made using a Raman spectrometer (NTEGRA Spectra, NT-MDT, Russia) with a 532 nm diode excitation laser, scanning electron microscopy using Tescan Mira 3LMU equipment, and X-ray photoelectron spectroscopy with a Thermo Fisher Scientific XPS NEXSA spectrometer.

Electrochemical Characterization. Electrochemical measurements were carried out using a potentiostat/galvanostat P-45X with an FRA-24 M impedance modulus (Electrochemical Instruments, Russia) using a three-electrode cell.

Gel-to-Gel Simulation. Gel-to-gel simulation was carried out using the same potentiostat. Two electrodes were contacted together using the textile soaked in saline (NaCl 0.9%) as a separator and gel model.

In Vivo Tests. Animal experiments were approved and performed according to the ISO 10993−10:2021 (Biological evaluation of medical devices—Part 10: Tests for skin sensitization) recommendations and guidelines from the Ethical Committee of the Siberian State Medical University, Tomsk, Russia (IACUC No. 7 from 7.09.2021).

Cell Proliferation. Mice-derived embryo fibroblast 3T3L1 cells (ATCC CL-173) were cultured in DMEM culture media (Paneco, Russia) supplemented with GlutaMAX (cell supplement #35050061, Gibco, TFS), 10% FBS, and antibiotics (penicillin/streptomycin mixture, Paneco, Russia).

Sweat Stability. Artificial sweat was prepared according to ISO 105-E04:2013. 0.5 g portion of monohydrate monohydrochloride L-histidine ($C_6H_9N_3O_2{\cdot}HCL{\cdot}H_2O$), 0.5 g of sodium chloride (NaCl), and 2.2 g of dihydrate sodium dihydrophosphate ($NaH_2PO_4{\cdot}2H_2O$) were added to 1 L of distilled water.

Washing stability test was performed using tap water with liquid soap with the addition of rubber balls.

All of the sheet resistance values were obtained by four-point probe measurements with a potentiostat/galvanostat P-45X with an FRA-24 M impedance modulus (Electrochemical Instruments, Russia) in the galvanostatic mode.

ECG, EMG, and EEG were recorded using an "Encifalan 131" (Medicom MTD, Russia). Ag/AgCl control electrode patches were purchased from FIAB Spa (Italy) and are certified medical devices in accordance with Regulation (EU) 2017/745 (MDR). The volunteer was a healthy man aged 51 years. Before installation, the skin was cleaned with 95% ethanol, following regulatory compliance and medical standards.

To record an ECG in lead I, the electrode was placed on the skin of the forearm and fixed with an adhesive patch. The electrodes were connected, as shown in Figure S17. To record an EMG, the graphene electrodes were placed proximally and distally on the flexor carpi radialis muscle and fixed with an adhesive patch. EEG recordings involved placing the graphene electrodes at the Fp1, Fp2, and A1 sites. Electrodes were secured by using an EEG cap.

The ECG, EMG, and EEG testing was conducted with the permission of Siberian State Medical University, Tomsk, Russia, Ethical Committee 7858/1 from 17.06.2020, with written consent by the participants.

Electrode aging was done by placing electrodes into a DPBS solution under constant heating at 37 °C for 6 days. ECG was recorded from the electrodes before and after aging, following the way described above.

■ ASSOCIATED CONTENT

Supporting Information

The Supporting Information is available free of charge at https://pubs.acs.org/doi/10.1021/acssensors.3c02361.

Additional experimental findings, including photos of the samples and experimental setups, electrochemical characterization of all of the samples, a summary of all of the parameters measured throughout the manuscript, a comparison of the rGO/PET/textile bioelectrode with the state-of-the-art, and a detailed explanation of the Methods and Materials used in this work (PDF)

■ AUTHOR INFORMATION

Corresponding Authors

Li Qiu − *Sichuan University, Chengdu 610041, China;* orcid.org/0000-0003-2685-9799; Email: qiulihx@scu.edu.cn

Raul D. Rodriguez − *Tomsk Polytechnic University, Tomsk 634050, Russia;* orcid.org/0000-0003-4016-1469; Email: raul@tpu.ru

Authors

Maxim Fatkullin − *Tomsk Polytechnic University, Tomsk 634050, Russia*

Vitaly Menzelintsev − *Tomsk Polytechnic University, Tomsk 634050, Russia*

Anna Lipovka − *Tomsk Polytechnic University, Tomsk 634050, Russia;* orcid.org/0000-0002-2012-1569

Elizaveta Dogadina − *Tomsk Polytechnic University, Tomsk 634050, Russia*

Evgenii Plotnikov − *Tomsk Polytechnic University, Tomsk 634050, Russia*

Konstantin Brazovskiy − *Tomsk Polytechnic University, Tomsk 634050, Russia*

Shuang Li − *College of Polymer Science and Engineering, State Key Laboratory of Polymer Materials Engineering, Department of Ultrasound, West China Hospital, Sichuan University, Chengdu 610065, China;* orcid.org/0000-0001-7414-630X

Lang Ma − *Sichuan University, Chengdu 610041, China;* orcid.org/0000-0003-3741-1885

Chong Cheng − *College of Polymer Science and Engineering, State Key Laboratory of Polymer Materials Engineering, Department of Ultrasound, West China Hospital, Sichuan University, Chengdu 610065, China;* orcid.org/0000-0002-6872-2240

Ekaterina Porokhova − *Laboratory of Cellular and Microfluidic Technologies, Siberian State Medical University, Tomsk 634050, Russia*

Igor Khlusov − *Laboratory of Cellular and Microfluidic Technologies, Siberian State Medical University, Tomsk 634050, Russia; Tomsk Polytechnic University, Tomsk 634050, Russia;* orcid.org/0000-0003-3465-8452

Evgeniya Sheremet − *Tomsk Polytechnic University, Tomsk 634050, Russia*

Complete contact information is available at: https://pubs.acs.org/10.1021/acssensors.3c02361

Author Contributions

M.F.: Conceptualization, methodology, formal analysis, investigation, data curation, validation, writing—original draft, writing—review and editing. V.M.: Formal analysis, investigation, data curation, validation, writing—review and editing, visualization. A.L.: Formal analysis, visualization, data curation, validation, writing—review and editing. E.D.: Formal analysis, investigation, data curation, visualization, writing—review and editing. E.P.: Methodology, investigation, resources, writing—review and editing. K.B.: Methodology, investigation, resources, writing—review and editing. S.L.: Formal analysis,

https://doi.org/10.1021/acssensors.3c02361
ACS Sens. 2024, 9, 1809−1819

writing—original draft, writing—review and editing. L.M.: Formal analysis, writing—original draft, writing—review and editing. C.C.: Formal analysis, writing—original draft, writing—review and editing. L.Q.: Formal analysis, writing—original draft, writing—review and editing. E.P.: Methodology, formal analysis, investigation, resources, writing—review and editing. I.K.: Methodology, formal analysis, investigation, resources, writing—review and editing. R.D.R.: Conceptualization, methodology, formal analysis, visualization, writing—original draft, writing—review and editing, visualization, supervision. E.S.: Conceptualization, methodology, formal analysis, writing—review and editing, supervision, resources, project administration, funding acquisition.

Notes

The authors declare no competing financial interest.

■ ACKNOWLEDGMENTS

This research was supported by the Priority project (Priority 2030-NIP/IZ-007-0000-2022 and Priority 2030-NIP/IZ-007-375-2023). This work was conducted using equipment from the Tomsk Regional Core Shared Research Facilities Center of National Research Tomsk State University. C. Cheng, S. Li, and L. Qiu acknowledge the financial support of the Supported by Sichuan Science and Technology Program (No. 2023YFH0008, 2023YFH0031, and 2023YFH0027). The authors thank the central laboratories of TPU (Analytical Center) for the XPS measurements and Alina Gorbunova for assistance with the experiments. The authors also thank Temur Nasibov and Anna Gorokhova, Siberian State Medical University, Tomsk, Russia, for their help designing and conducting biological tests.

■ REFERENCES

(1) Mishra, S.; Mohanty, S.; Ramadoss, A. Functionality of Flexible Pressure Sensors in Cardiovascular Health Monitoring: A Review. *ACS Sens* **2022**, *7* (9), 2495−2520.

(2) Tang, L.; Yang, J.; Wang, Y.; Deng, R. Recent Advances in Cardiovascular Disease Biosensors and Monitoring Technologies. *ACS Sens* **2023**, *8* (3), 956−973.

(3) Wan, J.; Gu, F.; Bao, W.; Dai, J.; Shen, F.; Luo, W.; Han, X.; Urban, D.; Hu, L. Sodium-Ion Intercalated Transparent Conductors with Printed Reduced Graphene Oxide Networks. *Nano Lett.* **2015**, *15* (6), 3763−3769.

(4) Mukherjee, R.; Thomas, A. V.; Krishnamurthy, A.; Koratkar, N. Photothermally Reduced Graphene as High-Power Anodes for Lithium-Ion Batteries. *ACS Nano* **2012**, *6* (9), 7867−7878.

(5) Zhang, Y.; Guo, L.; Wei, S.; He, Y.; Xia, H.; Chen, Q.; Sun, H.-B.; Xiao, F.-S. Direct Imprinting of Microcircuits on Graphene Oxides Film by Femtosecond Laser Reduction. *Nano Today* **2010**, *5* (1), 15−20.

(6) Park, S.; Ji, S.; Yoon, Y.; Kim, S. K.; Song, W.; Myung, S.; Lim, J.; Jung, H.-K.; Lee, S. S.; An, K.-S. Fabrication of Fanlike L-Shaped Graphene Nanostructures with Enhanced Thermal/electrochemical Properties via Laser Irradiation. *Carbon* **2021**, *182*, 691−699, DOI: 10.1016/j.carbon.2021.05.045.

(7) Kumar, R.; Joanni, E.; Singh, R. K.; da Silva, E. T. S. G.; Savu, R.; Kubota, L. T.; Moshkalev, S. A. Direct Laser Writing of Micro-Supercapacitors on Thick Graphite Oxide Films and Their Electrochemical Properties in Different Liquid Inorganic Electrolytes. *J. Colloid Interface Sci.* **2017**, *507*, 271−278.

(8) Zhou, X.-H.; Liu, L.-H.; Bai, X.; Shi, H.-C. A Reduced Graphene Oxide Based Biosensor for High-Sensitive Detection of Phenols in Water Samples. *Sens. Actuators, B* **2013**, *181*, 661−667.

(9) Pumera, M. Graphene in Biosensing. *Mater. Today* **2011**, *14* (7−8), 308−315.

(10) Sharma, S.; Pradhan, G. B.; Chhetry, A.; Shrestha, K.; Bhatta, T.; Zhang, S.; Kim, D.; Jeong, S.; Shin, Y.; Zahed, M. A.; Hui, X.; Park, J. Y. Graphene-Polymer Nanocomposites Electrode with Ionic Nanofibrous Membrane for Highly Sensitive Supercapacitive Pressure Sensor. *Nano Today* **2023**, *48*, No. 101698, DOI: 10.1016/j.nantod.2022.101698.

(11) Lipovka, A.; Fatkullin, M.; Shchadenko, S.; Petrov, I.; Chernova, A.; Plotnikov, E.; Menzelintsev, V.; Li, S.; Qiu, L.; Cheng, C.; Rodriguez, R. D.; Sheremet, E. Textile Electronics with Laser-Induced Graphene/Polymer Hybrid Fibers. *ACS Appl. Mater. Interfaces* **2023**, *15* (32), 38946−38955.

(12) Zhao, L.; Rosati, G.; Piper, A.; de Carvalho Castro, E.; Silva, C.; Hu, L.; Yang, Q.; Della Pelle, F.; Alvarez-Diduk, R. R.; Merkoçi, A. Laser Reduced Graphene Oxide Electrode for Pathogenic Escherichia Coli Detection. *ACS Appl. Mater. Interfaces* **2023**, *15* (7), 9024−9033, DOI: 10.1021/acsami.2c20859.

(13) Owda, A. Y.; Casson, A. J. *A Mini-Review of Graphene Based Materials for Electrodes in Electrocardiogram (ECG) Sensing*, 2021 IEEE International Conference on Flexible and Printable Sensors and Systems (FLEPS); IEEE, 2021 DOI: 10.1109/fleps51544.2021.9469827.

(14) Lipovka, A.; Petrov, I.; Fatkullin, M.; Murastov, G.; Ivanov, A.; Villa, N. E.; Shchadenko, S.; Averkiev, A.; Chernova, A.; Gubarev, F.; Saqib, M.; Sheng, W.; Chen, J.-J.; Kanoun, O.; Amin, I.; Rodriguez, R. D.; Sheremet, E. Photoinduced Flexible Graphene/polymer Nanocomposites: Design, Formation Mechanism, and Properties Engineering. *Carbon* **2022**, *194*, 154−161.

(15) Rodriguez, R. D.; Shchadenko, S.; Murastov, G.; Lipovka, A.; Fatkullin, M.; Petrov, I.; Tran, T.-H.; Khalelov, A.; Saqib, M.; Villa, N. E.; Bogoslovskiy, V.; Wang, Y.; Hu, C.-G.; Zinovyev, A.; Sheng, W.; Chen, J.-J.; Amin, I.; Sheremet, E. Ultra-robust Flexible Electronics by Laser-driven Polymer-nanomaterials Integration. *Adv. Funct. Mater.* **2021**, No. 2008818, DOI: 10.1002/adfm.202008818.

(16) Fatkullin, M.; Rodriguez, R. D.; Petrov, I.; Villa, N. E.; Lipovka, A.; Gridina, M.; Murastov, G.; Chernova, A.; Plotnikov, E.; Averkiev, A.; Cheshev, D.; Semyonov, O.; Gubarev, F.; Brazovskiy, K.; Sheng, W.; Amin, I.; Liu, J.; Jia, X.; Sheremet, E. Molecular Plasmonic Silver Forests for the Photocatalytic-Driven Sensing Platforms. *Nanomaterials* **2023**, *13* (5), 923 DOI: 10.3390/nano13050923.

(17) Murastov, G.; Bogatova, E.; Brazovskiy, K.; Amin, I.; Lipovka, A.; Dogadina, E.; Cherepnyov, A.; Ananyeva, A.; Plotnikov, E.; Ryabov, V.; Rodriguez, R. D.; Sheremet, E. Flexible and Water-Stable Graphene-Based Electrodes for Long-Term Use in Bioelectronics. *Biosens. Bioelectron.* **2020**, *166*, No. 112426.

(18) Shi, H.; Wang, C.; Sun, Z.; Zhou, Y.; Jin, K.; Redfern, S. A. T.; Yang, G. Tuning the Nonlinear Optical Absorption of Reduced Graphene Oxide by Chemical Reduction. *Opt. Express* **2014**, *22* (16), 19375−19385.

(19) Ma, B.; Rodriguez, R. D.; Ruban, A.; Pavlov, S.; Sheremet, E. The Correlation between Electrical Conductivity and Second-Order Raman Modes of Laser-Reduced Graphene Oxide. *Phys. Chem. Chem. Phys.* **2019**, *21* (19), 10125−10134.

(20) Roy, D.; Kanojia, S.; Mukhopadhyay, K.; Prasad, N. E. Analysis of Carbon-Based Nanomaterials Using Raman Spectroscopy: Principles and Case Studies. *Bull. Mater. Sci.* **2021**, *44* (1), No. 31, DOI: 10.1007/s12034-020-02327-9.

(21) Trusovas, R.; Ratautas, K.; Račiukaitis, G.; Barkauskas, J.; Stankevičienė, I.; Niaura, G.; Mažeikienė, R. Reduction of Graphite Oxide to Graphene with Laser Irradiation. *Carbon N. Y.* **2013**, *52*, 574−582.

(22) Evlashin, S. A.; Svyakhovskiy, S. E.; Fedorov, F. S.; Mankelevich, Y. A.; Dyakonov, P. V.; Minaev, N. V.; Dagesyan, S. A.; Maslakov, K. I.; Khmelnitsky, R. A.; Suetin, N. V.; Akhatov, I. S.; Nasibulin, A. G. Ambient Condition Production of High Quality Reduced Graphene Oxide. *Adv. Mater. Interfaces* **2018**, *5* (18), No. 1800737, DOI: 10.1002/admi.201800737.

(23) Chen, X.; Wang, X.; Fang, D. A Review on C1s XPS-Spectra for Some Kinds of Carbon Materials. *Fullerenes, Nanotubes Carbon Nanostruct.* **2020**, *28* (12), 1048−1058.

(24) Boehler, C.; Carli, S.; Fadiga, L.; Stieglitz, T.; Asplund, M. Tutorial: Guidelines for Standardized Performance Tests for Electrodes Intended for Neural Interfaces and Bioelectronics. *Nat. Protoc.* **2020**, *15* (11), 3557−3578.
(25) Shao, Y.; Wang, J.; Engelhard, M.; Wang, C.; Lin, Y. Facile and Controllable Electrochemical Reduction of Graphene Oxide and Its Applications. *J. Mater. Chem.* **2010**, *20* (4), 743−748.
(26) Hamed, A.; Hessein, A.; Abd El-Moneim, A. Towards High Performance Flexible Planar Supercapacitors: In-Situ Laser Scribing Doping and Reduction of Graphene Oxide Films. *Appl. Surf. Sci.* **2021**, *551*, No. 149457, DOI: 10.1016/j.apsusc.2021.149457.
(27) Zhang, R.; Palumbo, A.; Kim, J. C.; Ding, J.; Yang, E.-H. Flexible Graphene-, Graphene-oxide-, and Carbon-nanotube-based Supercapacitors and Batteries. *Ann. Phys.* **2019**, *531* (10), No. 1800507, DOI: 10.1002/andp.201800507.
(28) Eng, A. Y. S.; Ambrosi, A.; Chua, C. K.; Saněk, F.; Sofer, Z.; Pumera, M. Unusual Inherent Electrochemistry of Graphene Oxides Prepared Using Permanganate Oxidants. *Chemistry* **2013**, *19* (38), 12673−12683.
(29) McAdams, E. Bioelectrodes. In *Encyclopedia of Medical Devices and Instrumentation*; John Wiley & Sons, Inc: Hoboken, NJ, USA, 2006 DOI: 10.1002/0471732877.emd013.
(30) Cohn, A. P.; Share, K.; Carter, R.; Oakes, L.; Pint, C. L. Ultrafast Solvent-Assisted Sodium Ion Intercalation into Highly Crystalline Few-Layered Graphene. *Nano Lett.* **2016**, *16* (1), 543−548.
(31) Share, K.; Cohn, A. P.; Carter, R. E.; Pint, C. L. Mechanism of Potassium Ion Intercalation Staging in Few Layered Graphene from in Situ Raman Spectroscopy. *Nanoscale* **2016**, *8* (36), 16435−16439.
(32) Dallavalle, M.; Calvaresi, M.; Bottoni, A.; Melle-Franco, M.; Zerbetto, F. Graphene Can Wreak Havoc with Cell Membranes. *ACS Appl. Mater. Interfaces* **2015**, *7* (7), 4406−4414.
(33) Seabra, A. B.; Paula, A. J.; de Lima, R.; Alves, O. L.; Durán, N. Nanotoxicity of Graphene and Graphene Oxide. *Chem. Res. Toxicol.* **2014**, *27* (2), 159−168.
(34) Pinto, A. M.; Gonçalves, I. C.; Magalhães, F. D. Graphene-Based Materials Biocompatibility: A Review. *Colloids Surf., B* **2013**, *111*, 188−202.
(35) Yun, Y. J.; Ju, J.; Lee, J. H.; Moon, S.-H.; Park, S.-J.; Kim, Y. H.; Hong, W. G.; Ha, D. H.; Jang, H.; Lee, G. H.; Chung, H.-M.; Choi, J.; Nam, S. W.; Lee, S.-H.; Jun, Y. Highly Elastic Graphene-based Electronics toward Electronic Skin. *Adv. Funct. Mater.* **2017**, *27* (33), No. 1701513, DOI: 10.1002/adfm.201701513.
(36) Carneiro, M. R.; Majidi, C.; Tavakoli, M. Multi-electrode Printed Bioelectronic Patches for Long-term Electrophysiological Monitoring. *Adv. Funct. Mater.* **2022**, *32* (43), No. 2205956, DOI: 10.1002/adfm.202205956.
(37) Pani, D.; Achilli, A.; Bonfiglio, A. Survey on Textile Electrode Technologies for Electrocardiographic (ECG) Monitoring, from Metal Wires to Polymers. *Adv. Mater. Technol.* **2018**, *3* (10), No. 1800008, DOI: 10.1002/admt.201800008.

https://doi.org/10.1021/acssensors.3c02361
ACS Sens. 2024, 9, 1809−1819